

# UC Berkeley

## UC Berkeley Previously Published Works

**Title**

Simulating bioclogging effects on dynamic riverbed permeability and infiltration

**Permalink**

<https://escholarship.org/uc/item/7hp2p9c4>

**Journal**

Water Resources Research, 52(4)

**ISSN**

0043-1397

**Authors**

Newcomer, Michelle E  
Hubbard, Susan S  
Fleckenstein, Jan H  
[et al.](#)

**Publication Date**

2016-04-01

**DOI**

10.1002/2015wr018351

Peer reviewed



## RESEARCH ARTICLE

10.1002/2015WR018351

## Key Points:

- Riverbed bioclogging is a key control on infiltration in losing rivers
- River infiltration gains from disconnection can offset riverbed permeability declines caused by bioclogging
- Permeability reduction can hasten the onset of disconnection

## Supporting Information:

- Supporting Information S1
- Data Set S1

## Correspondence to:

Y. Rubin,  
rubin@ce.berkeley.edu

## Citation:

Newcomer, M. E., S. S. Hubbard, J. H. Fleckenstein, U. Maier, C. Schmidt, M. Thullner, C. Ulrich, N. Flipo, and Y. Rubin (2016), Simulating bioclogging effects on dynamic riverbed permeability and infiltration, *Water Resour. Res.*, 52, doi:10.1002/2015WR018351.

Received 7 NOV 2015

Accepted 14 MAR 2016

Accepted article online 18 MAR 2016

## Simulating bioclogging effects on dynamic riverbed permeability and infiltration

Michelle E. Newcomer<sup>1,2</sup>, Susan S. Hubbard<sup>3</sup>, Jan H. Fleckenstein<sup>2</sup>, Ulrich Maier<sup>2</sup>, Christian Schmidt<sup>2</sup>, Martin Thullner<sup>4</sup>, Craig Ulrich<sup>3</sup>, Nicolas Flipo<sup>5</sup>, and Yoram Rubin<sup>1</sup>
<sup>1</sup>Department of Civil and Environmental Engineering, University of California, Berkeley, Berkeley, California, USA, <sup>2</sup>UFZ-Helmholtz Centre for Environmental Research, Department of Hydrogeology, Leipzig, Germany, <sup>3</sup>Lawrence Berkeley National Laboratory, Earth Sciences Division, Berkeley, California, USA, <sup>4</sup>UFZ-Helmholtz Centre for Environmental Research, Department of Environmental Microbiology, Leipzig, Germany, <sup>5</sup>Geosciences Department, MINES ParisTech, PSL Research University, Paris, France

**Abstract** Bioclogging in rivers can detrimentally impact aquifer recharge. This is particularly so in dry regions, where losing rivers are common, and where disconnection between surface water and groundwater (leading to the development of an unsaturated zone) can occur. Reduction in riverbed permeability due to biomass growth is a time-variable parameter that is often neglected, yet permeability reduction from bioclogging can introduce order of magnitude changes in seepage fluxes from rivers over short (i.e., monthly) timescales. To address the combined effects of bioclogging and disconnection on infiltration, we developed numerical representations of bioclogging processes within a one-dimensional, variably saturated flow model representing losing-connected and losing-disconnected rivers. We tested these formulations using a synthetic case study informed with biological data obtained from the Russian River, California, USA. Our findings show that modeled biomass growth reduced seepage for losing-connected and losing-disconnected rivers. However, for rivers undergoing disconnection, infiltration declines occurred only after the system was fully disconnected. Before full disconnection, biologically induced permeability declines were not significant enough to offset the infiltration gains introduced by disconnection. The two effects combine to lead to a characteristic infiltration curve where peak infiltration magnitude and timing is controlled by permeability declines relative to hydraulic gradient gains. Biomass growth was found to hasten the onset of full disconnection; a condition we term ‘effective disconnection’. Our results show that river infiltration can respond dynamically to bioclogging and subsequent permeability declines that are highly dependent on river connection status.

## 1. Introduction

The ability to accurately predict infiltration from rivers and recharge of water to nearby groundwater aquifers is essential to water resources management [Crosbie *et al.*, 2014; Harvey and Gooseff, 2015]. Riverbank Filtration (RBF) systems (Figure 1), typically used for the production of drinking water, make use of high infiltration capacities in addition to passive filtration benefits provided by river systems [Jaramillo, 2012; McCallum *et al.*, 2013]. Accurate management of RBF pumping strategies requires information about infiltration dynamics, which depend on characterization of sediment properties and their temporal variability, such as streambed permeability. Although field measurements indicate that riverbed permeability is often dynamic, due to processes such as subsurface bioclogging and sedimentation [Annan, 2001; Blaschke *et al.*, 2003; Doppler *et al.*, 2007; Genereux *et al.*, 2008; Hatch *et al.*, 2010; Engeler *et al.*, 2011; Zhang *et al.*, 2011; Kurtz *et al.*, 2012; Taylor *et al.*, 2013], most surface-groundwater numerical models assume that it is constant over time [Doppler *et al.*, 2007; Flipo *et al.*, 2014]. Ignoring these dynamic processes in predictive numerical models could have significant ramifications for practical management of water resources, especially in drought-prone regions where losing rivers are common.

Subsurface bioclogging can affect pore scale sediment permeability and porosity through river system ecological processes and surface-groundwater interactions [Battin and Sengschmitt, 1999]. Biofilms are aggregates of microbial biomass that consist of bacterial cells and exopolymeric saccharides (EPS) produced by these cells [Wingender *et al.*, 1999; Or *et al.*, 2007]. These aggregates can occupy pore throats and pore

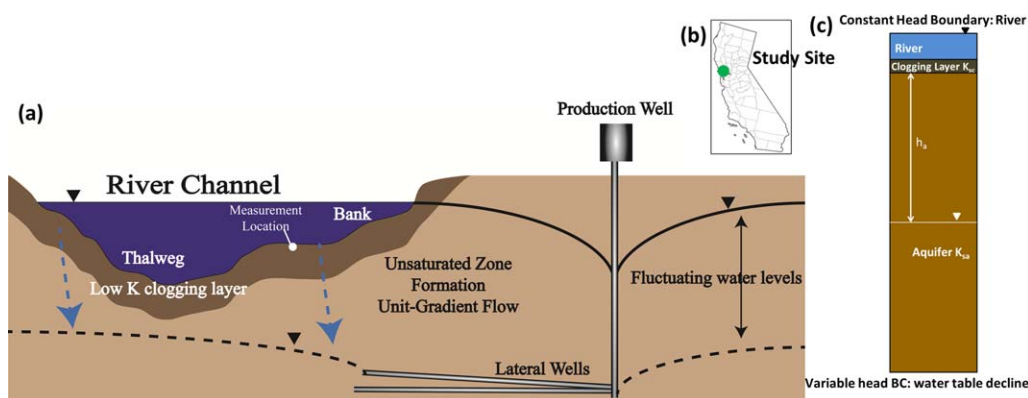


**Figure 1.** (a) Conceptual, two-dimensional diagram of a river and key aspects that govern infiltration, based on the Wohler RBF site in CA. The figure illustrates aspects such as riverbed clogging layer (low conductivity layer), aquifer layer, fluctuating water table, unsaturated zone formation (disconnection), location of unit-gradient (UG) flow, RBF well location, and lateral pumping wells. (b) Location map of the Wohler RBF site in California, whose data inspired this study (Lat: 38.5, Long:  $-122.9$ ). (c) One-dimensional profile of the layered sediments at a general location within the river cross section where the flow path is dominantly vertical and where disconnection occurs. Note: This figure is not to scale. Lateral wells are located sufficiently below the river that all flow paths are dominantly vertical from the river, even those in the unsaturated zone.

spaces, thereby decreasing hydraulic conductivity by orders of magnitude through physical clogging [Baveye *et al.*, 1998; Rockhold *et al.*, 2002; Thullner, 2010]. Although many models represent microbial growth and decay as a function of nutrient substrates [Molz *et al.*, 1986; Murphy and Ginn, 2000; Thullner *et al.*, 2007], most model approaches describing bioclogging are pore-scale models [e.g., Suchomel *et al.*, 1998; Kim *et al.*, 2000; Dupin *et al.*, 2001; Thullner *et al.*, 2002a; Thullner and Baveye, 2008; Ezeuko *et al.*, 2011; Rosenzweig *et al.*, 2014]. Few of these incorporate scaled-up representations of bioclogging processes [Kildsgaard and Engesgaard, 2001; Thullner *et al.*, 2004; Brovelli *et al.*, 2009; Soleimani *et al.*, 2009; Samsó *et al.*, 2016] that are required to simulate bioclogging influences on river system behavior.

Accurate prediction of infiltration from a losing river depends on the status of river-aquifer connection as well as dynamic streambed permeability. Rivers can be hydraulically connected to an aquifer (with no unsaturated zone beneath the riverbed, low hydraulic gradients, and minimal vertical seepage), or they can be hydraulically disconnected (with a fully developed unsaturated zone, unit-gradient (UG) flow, and maximum seepage) [Fox and Durnford, 2003; Brunner *et al.*, 2009a; Rivière *et al.*, 2014]. The process of disconnection begins when groundwater levels drop, such as from pumping or long periods of drought (Figure 1). When rivers are fully disconnected, further groundwater level drops no longer affect the infiltration rate. Although several studies have documented dynamics in riverbed permeability and river-aquifer connection separately [Treese *et al.*, 2009; Hatch *et al.*, 2010; Lamontagne *et al.*, 2011], their coupled influence on infiltration has not been fully evaluated. Confounding indications from field measurements, which show seepage increases concurrent with riverbed permeability declines, motivate the development of models that can account for transient river-aquifer connection [Hatch *et al.*, 2010; Zhang *et al.*, 2011; Ulrich *et al.*, 2015].

In this study, we assess the controlling mechanisms of infiltration in a losing river under conditions of subsurface bioclogging using a synthetic case study inspired by field data from the Russian River near Wohler, California, USA. We use a generic one-dimensional profile to demonstrate bioclogging effects on long-term infiltration trends to emphasize the applicability of this approach to other rivers where bioclogging and disconnection may dominate. We evaluate the effects of bioclogging on infiltration trends, timing of peak infiltration, and the evolution of unsaturated zone profiles from losing-connected to losing-disconnected river conditions. Our main goal is to isolate two important monthly/seasonal scale processes that, when combined, can reproduce observed temporal trends. To our knowledge, bioclogging and assessment of temporally dynamic parameters on infiltration in field scenarios have not been analyzed sufficiently in the literature, which motivates this study. This predictive ability is critical for optimal management of pumping in drought-prone areas, especially over long time frames where feedback effects may become important [Treese *et al.*, 2009; Hatch *et al.*, 2010]. This work aims to bridge the gap between hydrological and ecohydrological views of the stream-aquifer interface by incorporating pore-scale representations of

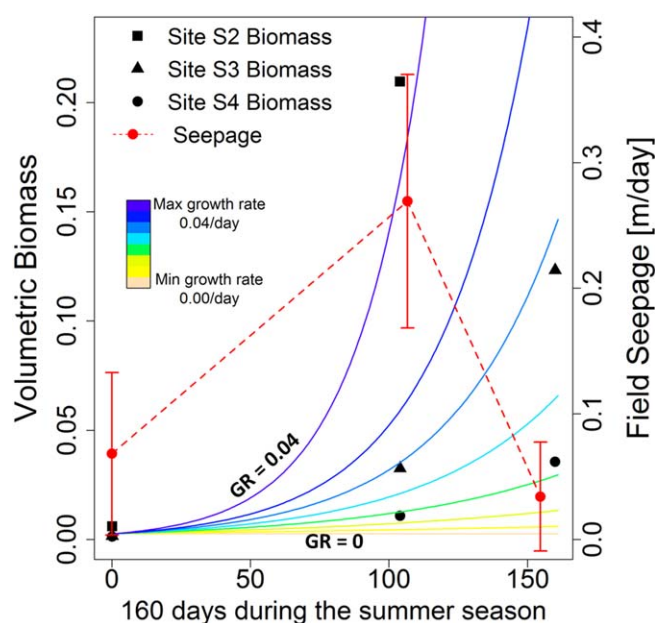


**Figure 2.** Field values of seepage measured and averaged across multiple locations. The red dashed line connects seepage measurements made during three field campaigns; error bars show the large variability between sites. Field values of volumetric biomass are shown at three locations. Predicted exponential biomass growth curves range across many growth rates. Volumetric biomass is the ratio of the biomass volume relative to the volume of the sediment sample. Different curves over the range of biomass growth rates (GR) are shown. For the color versions of these figures, the reader is referred to the electronic version of this article. Seepage data can be found in the supporting information for this article online.

bioclogging processes into local-scale models of river system infiltration to account for temporal variability found in natural settings.

## 2. Wohler Study Site, Previous Modeling, and Data Sets Used

Located along the Russian River in Sonoma County, CA, USA, the Sonoma County Water Agency (SCWA) Wohler site provides drinking water to 600,000 people annually. To provide this water, collector wells located on the riverbank use lateral wellbores that extend at depth toward the river to pump water that has infiltrated from the river downward through sediments (Figure 1). The total production capacity of the SCWA RBF facility is estimated to be  $\sim 350,000 \text{ m}^3$  per day (92 million gallons per day). Prior studies have estimated riverbed infiltration rates ranging between 0.1–1 m/d at various locations along the Russian River [Harding Lawson Associates, 1988]. During peak demand months, SCWA raises

an inflatable dam on the Russian River downstream of the Wohler site to increase infiltration. On-off pumping cycles, as well as the rate of daily pumping, can change the water table position on a daily and subdaily timescale. Pumping over the entire summer season leads to a large, regional water table drop. A conceptual one-dimensional and two-dimensional schematic of the river system, including the river, the riverbed clogging layer, and the fluctuating groundwater level, is shown in Figure 1. The clogging layer represents a sediment boundary where an inverted water table (i.e., a saturated zone overlies an unsaturated zone) can potentially form [Dillon and Liggett, 1983; Peterson, 1989; Xie et al., 2013; Rivière et al., 2014].

Both numerical and experimental studies have been performed at the Wohler Site to aid RBF operations. Experimental studies along the Russian River and Pajaro River (150 km south of the Russian River) have documented that infiltration did not simply decline with riverbed permeability: in some cases, measured flux was found to increase when permeability decreased [Su et al., 2007; Hatch et al., 2010; Ulrich et al., 2015]. Numerical, two-dimensional simulations and inversions for riverbed permeability at the Wohler site indicated a strong, dynamic component that had not previously been accounted for in models of infiltration [Su et al., 2007; Zhang et al., 2011]. These models did not account for bioclogging-induced permeability effects, or for simultaneous river disconnection.

Motivated by these simulation results, extensive field campaigns were conducted in 2012 to investigate spatio-temporal controls on riverbed clogging processes [Ulrich et al., 2015]. Here, we use three of the data sets collected during those campaigns to inform and compare with model results: (1) grain size distributions (GSD) from 38 sediment samples used for estimating porosity from five riverbed sites, (2) subsurface biomass from cryocores analyzed using the phospholipid fatty acid technique at three of the five sites [White and Ringelberg, 1998] (Figure 2), and (3) spatially averaged seepage from seepage meters collected at four of the sites (Figure 2). Large variability in the seepage data indicates that infiltration in different parts of the river may be subject to spatially variable disconnection or clogging at different times. Riverbed sediments were collected to a depth of 0.2 m during spring, summer, and fall of 2012. Cryocoring techniques were used to preserve the structural and biological integrity of the riverbed sediment samples during transport

to the laboratory. All samples were collected along the bank of the river cross section. Data were collected during 5 months, May through November, which represent the time period (160 days) when bioclogging is most relevant. An important finding of the *Ulrich et al.* [2015] study was that biotic processes play a much larger role in riverbed clogging at the Wohler site relative to abiotic processes (e.g., sedimentation and erosion; see *Blaschke et al.* [2003]). We focus on riverbed clogging by biofilms because of the potential for significant decreases in permeability over relatively short time periods (i.e., one summer season).

Analysis of the data described above, as well as other Wohler data sets, revealed key spatial and temporal characteristics of the study site [*Ulrich et al.*, 2015]. Riverbed sediments contained gravels and cobbles with a sandy-silt matrix. Bacterial, fungal, algal, and general plant biomass cells per gram of sediment ranged from  $10^4$  cells/gram-dry-weight in the spring to  $10^7$  cells/gram-dry-weight in the late summer. Biomass concentrations are similar to those reported in *Gupta and Swartzendruber* [1962] and *Seki et al.* [2006]. Another important finding from *Ulrich et al.* [2015] was the development of a laterally extensive unsaturated zone midway through the summer, shown using time-lapse Electrical Resistivity Tomography (ERT) images. Average seepage values from multiple sites (represented by white dots in Figure 1), from the end of May until November 2012 (160 days), show that the seepage increased midway through the summer, then decreased to almost zero by the end of the summer (Figure 2). This seepage trend is consistent with the hypothesis that the system initially experiences disconnection (predicting seepage increases), followed by bioclogging limitations thereafter. To our knowledge, this is the first observation of disconnection in a real river. Additional details about the data sets are provided in *Ulrich et al.* [2015].

### 3. Methods

#### 3.1. Biomass Growth and Volume Fraction

Continuous biomass growth curves (Figure 2) were calculated using a first-order exponential model fitted to the biomass field data obtained from the top of the field core ( $\mu\text{g g}^{-1}$  dry weight). Decay, sorption, and grazer consumption were ignored; therefore this represents a very simplified growth model. The first-order exponential model of biomass growth is given by:

$$\frac{dX}{dt} = \mu X \quad (1)$$

$X$  is the mass (dry weight) of biomass per unit mass of solids ( $\mu\text{g g}^{-1}$ ), and  $\mu$  is the specific growth rate with units of day. A range of effective biomass growth rates fit to the field data were used ( $\mu = 0.005\text{--}0.04$  day). An initial value of biomass ( $A_0$ ) was set at  $0.4 \mu\text{g g}^{-1}$ . Growth rates found in the literature can range by many orders of magnitude and are typically used with Monod kinetic reactions [*Murphy and Ginn*, 2000; *Brun and Engesgaard*, 2002; *Thullner et al.*, 2007]. For our simulations, we did not use Monod kinetics because of the lack of nutrient data, and because our aim was to constrain the model with true biomass field data.

Each biomass growth model was converted to a time-series of relative porosity using equations (2)–(5). A porosity associated with each grain-size distribution was calculated using equations (2) and (3). The original porosity ( $n_0$ ) was obtained from the field-sampled grain size distributions, where  $d_{10}$  represents the grain size (mm) at which 10% of the data fall below, and similarly for  $d_{60}$  [*Barahona-Palomo et al.*, 2011]:

$$n_0 = 0.255 * (1 + 0.83^U) \quad (2)$$

$$U = \frac{d_{60}}{d_{10}} \quad (3)$$

From the 38 grain size distributions, the mean porosity was 0.276 and standard deviation was 0.017.

Biomass volumetric fraction ( $n_{bio}$ ) was calculated with equation (4):

$$n_{bio} = \frac{X_s \rho_b}{\rho_s} \quad (4)$$

In this equation,  $X_s$  is the mass (dry weight) of the biomass per unit mass of solids ( $\mu\text{g/g}$ ), the bulk density of the porous medium is given by  $\rho_b$ , and the density of the average biomass is given by  $\rho_s$  which represents

**Table 1.** Parameter Set for the Biofilm and Colonies Models [Thullner et al., 2002]

Biofilm		Colonies	
$K_{min}$	$n_r^0$	$a$	$n_r^0$
0.008	0.3	−1.8	0.8

a sum of all the microorganisms—bacteria, algae, fungi, EPS, etc. Units for  $\rho_b$  and  $\rho_s$  are given in  $\text{kg m}^{-3}$ . Bulk density of the riverbed sediments ( $\rho_b$ ) and density of the biomass ( $\rho_s$ ) were unknown, and thus were selected from the range of values published in the literature ( $\rho_b = 1600$  ( $\text{kg m}^{-3}$ ) is a typical value for sands, and  $\rho_s = 0.25\text{--}2.5$  ( $\text{kg m}^{-3}$  dry mass/wet volume))

[Coughlan et al., 2002; Thullner et al., 2004; Rockhold et al., 2005; Brown and Wherrett, 2014; Rosenzweig et al., 2014]. Biomass volume fraction times-series for each growth rate are shown in Figure 2.

Relative porosity ( $n_r$ ), shown by equation (5), expresses the new porosity given biomass growth relative to the original porosity, and is given by the ratio of the updated porosity ( $n_{new} = n_0 - n_{bio}$ ) to the original porosity ( $n_0$ ).

$$n_r = \frac{n_0 - n_{bio}}{n_0} = \frac{n_{new}}{n_0} \quad (5)$$

### 3.2. Dynamic Permeability Functions

To link biomass growth models over time (cf. Figure 2) to a clogging potential represented by a hydraulic conductivity drop, we used the Colonies and Biofilm constitutive models [Thullner et al., 2002] shown in equations (6) and (8) with previously published parameters from pore-network simulations (Table 1) [Thullner et al., 2002a]. We use both Colonies and Biofilm models because they have been tested against experimental data and show acceptable performance [Thullner, 2010], and because there is no general agreement in the literature which model is most adequate. These two models represent a reasonable range of the degree of bioclogging a system may experience.

The Colonies model, conceptualized as aggregates of biomass within the pore-space, is given as:

$$K_r(n_r) = a \left( \frac{n_r - n_r^0}{1 - n_r^0} \right)^3 + (1 - a) \left( \frac{n_r - n_r^0}{1 - n_r^0} \right)^2 \quad (6)$$

In equation (6), parameters include  $n_r^0$  and  $a$ . Values for  $n_r^0$  range from 0 to 1, and represent the value of the relative porosity at which the relative saturated hydraulic conductivity asymptotically approaches a minimum. The parameter  $a$  represents a functional weight of the conductivity decline. Relative porosity ( $n_r$ ) from equation (5) is an input to equation (6).  $K_r(n_r)$  is the relative saturated hydraulic conductivity given by the ratio of the updated saturated hydraulic conductivity ( $K_{sc,new}$ ) of the riverbed sediment clogging layer, to the original saturated hydraulic conductivity ( $K_{sc}$ ) of that same layer:

$$K_r(n_r) = \frac{K_{sc,new}}{K_{sc}} \quad (7)$$

The Biofilm model, conceptualized as a film enveloping each sediment grain, is given as:

$$K_r(n_r) = \left[ \left( \frac{n_r - n_r^0}{1 - n_r^0} \right)^{1.8} + K_{min} \right] \frac{1}{1 + K_{min}} \quad (8)$$

In the Biofilm model,  $K_r$ ,  $n_r$ , and  $n_r^0$  are the same as the Colonies model, and  $K_{min}$  is a parameter describing the residual relative conductivity of a fully clogged medium. The Biofilm and Colonies models are shown in Figure 3a, which shows the degree of clogging and conductivity decline for each.

Dynamic permeability functions representing changes over time in hydraulic conductivity from biomass growth (solutions to equations (6) and (8)) are shown as continuous functions over time in Figure 3b, and are represented by the relative hydraulic conductivity  $K_r(n_r)$ . Marginal probability density functions (pdfs) of  $K_r(n_r)$  by season are shown in Figure 3c. Once  $K_r(n_r)$  was found, equation (7) could be rearranged to solve for  $K_{sc,new}$  given an initial condition for  $K_{sc}$ . All permeability models shown in Figure 3b were supplied as inputs to the HYDRUS-1D numerical code as daily updates of the clogging layer conductivity and porosity ( $K_{sc,new}$  and  $n_{new}$ ).



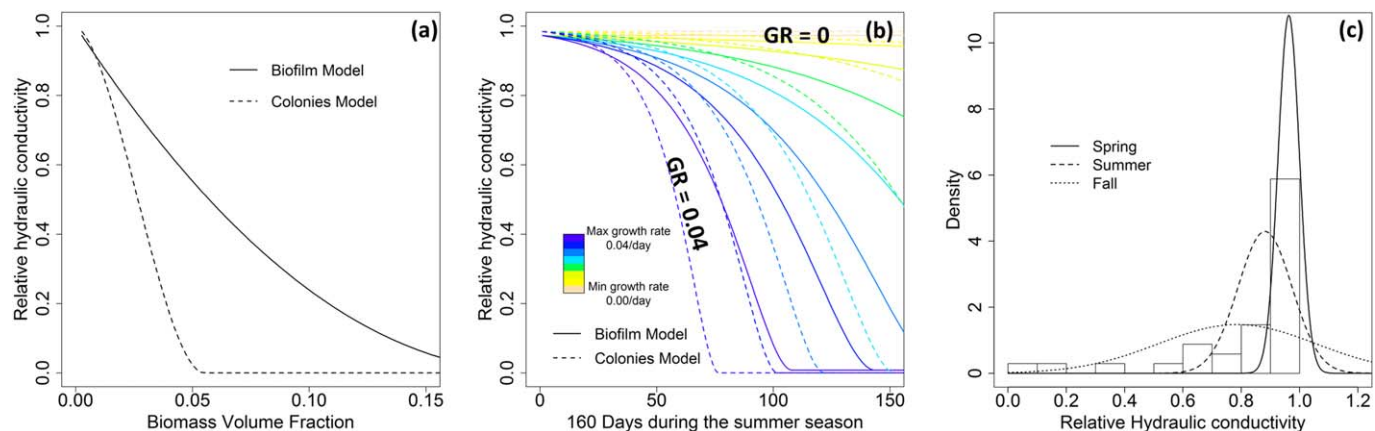


**Figure 3.** (a) Biofilm constitutive model (solid line) and Colonies constitutive model (dashed line) link a biomass volume fraction to a hydraulic conductivity decrease. (b) Dynamic permeability functions are shown over time. Different curves over the range of biomass growth rates (GR) are shown. (c) Fitted marginal probability density functions (pdfs) of the relative hydraulic conductivity estimates from the field biomass data for each season. For interpretation of the color in all figure legends, the reader is referred to the web version of this article.

### 3.3. Numerically Linking the Bioclogging Models and HYDRUS-1D

Inspired by the Wohler CA field infiltration data, we implemented two main processes within the modeling framework to test our hypothesis that disconnection and bioclogging cooccur to produce the long-term infiltration trend (Figure 2): (1) time-dependent parameters calculated from the field bioclogging data, and (2) a time-dependent, lower head boundary condition to induce disconnection (representing the effects of pumping).

#### 3.3.1. Time-Dependent Parameters

We generated time series of parameters  $n_{new}$  and  $K_{sc,new}$  from the field data according to equations (5)–(8). A time series of decreases in hydraulic conductivity due to bioclogging are shown in Figure 3b. We generated these time series using the bioclogging field data (Figure 2), the sediment GSD for the initial porosity values ( $n_0$ , equation (2)), the biological growth models (fast or slow growth rates) (Figure 2, equation (1)), and the clogging constitutive models (Biofilm and Colonies) described by equations (6)–(8) and shown in Figure 3a. These time series were used as time-dependent parameterization for the riverbed clogging layer (Figure 1c), and updated within the HYDRUS-1D numerical models using a daily update scheme described below.

#### 3.3.2. Time-Dependent Lower Head Boundary

We examined two types of rivers showing the end-members of the disconnection spectrum: (1) a river undergoing disconnection from fast water table declines, and (2) a river remaining connected from slow water table declines. Water table decline rates imposed in the HYDRUS-1D model are ideal, linear representations of pumping effects on local water levels over the course of the summer months. Local observation wells show much variability in water levels from on-off pumping cycles. Our goal was not to simulate the random water table fluctuations from high-frequency pumping cycles, but instead to represent the overall summer water table decline trend. Fast water table declines can be conceptualized as the highest pumping rates, and slow water table declines can be conceptualized as low/moderate pumping rates. Four different rates of water table decline between the two end-members defined above were used: 0.03, 0.06, 0.15, and 0.59 cm d<sup>−1</sup>. From each water table decline rate, we generated a time series of daily head values to update the lower boundary condition of the numerical model (Figure 1c). Fast water table drops allowed the system to disconnect quickly, and showed greater change in storage (unsaturated zone development) before significant bioclogging occurred, while slow water table drops allowed the system to remain connected during bioclogging.

#### 3.3.3. HYDRUS-1D

Modeling consisted of a series of two autonomous models that were loosely coupled: HYDRUS-1D transient simulations, and our time-dependent bioclogging parameterization [Simunek et al., 2008; PC-Progress, 2011]. Since HYDRUS-1D does not have bioclogging capabilities, we used a loosely-coupled modeling approach to synchronize our bioclogging data at each time step within HYDRUS-1D. Loosely-coupled approaches allow the exchange of sequenced output data from autonomous models, and may address some of the reported difficulties (for a detailed description, see Alarcon et al. [2014]) of representing pore-scale processes in fully-coupled, local-to-continuum-scale flow models [Tang et al., 2015].

**Table 2.** van Genuchten Parameters Supplied as Initial Values to the Layers in the Synthetic HYDRUS-1D Model [van Genuchten, 1980]<sup>a</sup>

Layer	Depth (m)	$\theta_r$	$\theta_s$	$\alpha$ (m <sup>-1</sup> )	$n$	$I$ (m <sup>-1</sup> )	$K_s$ (m/d)
Clogging Layer	0–0.1	0.078	0.27	3.6	1.56	0.5	0.205
Aquifer	0.1–1	0.045	0.43	14.5	2.68	0.5	20–100

<sup>a</sup>Parameters for the residual water content ( $\theta_r$ ), the saturated water content ( $\theta_s$ ), a measure of the inverse air-entry suction ( $\alpha$ ), a measure of the porosity distribution ( $n$ ), a constant parameter ( $I$ ), and saturated hydraulic conductivity ( $K_s$ ) can be found from the Rosetta database [Schaap *et al.*, 2001].

The lower pressure head, porosity, and saturated hydraulic conductivity ( $K_{sc, new}$ ) were updated daily within the numerical model during the 160 day simulation period. We updated the lower pressure head at the bottom boundary to represent a water table decline from pumping. All transient parameters were applied to the model as daily averages. Each daily simulation was updated with new parameters at the beginning of the new day. Initial conditions with the previous day's steady state pressure heads were imposed on the next simulation, and approximated the new steady state after a few hours. Model test runs using 0.5 day conductivity update time steps produced identical fluxes over the simulation period, confirming insensitivity to the time steps at which the conductivity was updated. This approach is justified because conductivity changes from bioclogging occur gradually each day over the entire summer season.

### 3.3.4. Synthetic Domain

The synthetic one-dimensional domain consists of two sediment layers representing the riverbed clogging layer (0.1 m) and the aquifer layer (0.9 m) (Figure 1c), initialized with hydraulic conductivity values characteristic of typical values for loam and sand, respectively (Table 2), and represents a generic location within the river-aquifer cross section (Figure 1a). The inclusion of temporal variations in riverbed hydraulic conductivity is an extension of the model described by Brunner *et al.* [2009a], which is a well-established reference case in the literature (Figure 1c). Depth of ponded water ( $d$ ) was 0.2 m. The domain was discretized with a grid spacing of 0.001 m, with initial pressure head conditions linearly varying between 0.2 m (top) and 0.95 m (bottom) representing completely connected, and losing initial conditions. This choice of initially losing conditions arbitrarily starts our model at values of infiltration larger than 0. The field data of seepage (Figure 2) shows some starting infiltration values around 0. We believe this is because in winter and early spring groundwater may discharge into the river. We start our models with fully losing conditions rather than gaining to save model run time. The van Genuchten parameters used in the van Genuchten-Mualem water retention functions in HYDRUS-1D are provided in Table 2 [van Genuchten, 1980]. A total of 192 simulations were run representing different combinations of growth rate parameters ( $\mu = 0.005$ – $0.04$  day<sup>-1</sup>), rate of water table drop to represent fast or slow pumping ( $0.03$ – $0.59$  cm d<sup>-1</sup>), aquifer conductivity ( $20$ – $100$  m d<sup>-1</sup>), and constitutive model (Biofilm or Colonies).

Using a one-dimensional simplification of a two-dimensional groundwater-surface water conceptual model and a sufficiently small capillary zone, Brunner *et al.* [2009a] presented a theoretical development to approximate the context for the occurrence of disconnection:

$$\frac{K_{sc}}{K_{sa}} \leq \frac{h_c}{d + h_c} \quad (9)$$

Here  $K_{sc}$  is the saturated hydraulic conductivity of the riverbed clogging layer [L T<sup>-1</sup>],  $K_{sa}$  is the saturated hydraulic conductivity of the aquifer [L T<sup>-1</sup>],  $h_c$  is the thickness of the clogging layer [L], and  $d$  is the depth of ponded water [L] [Brunner *et al.*, 2009a, 2011]. Brunner *et al.* [2009a] approximated local unit-gradient (UG) conditions at the time of maximum infiltration between the clogging layer and the water table represented by a pressure head = 0, leading to an approximation of the total head as  $dH/dz_a \approx 1$ , where  $H$  is total head [L] and  $z_a$  is elevation [L]. The approximation of UG conditions does not allow for nonlinear effects of  $dH/dz_a$  in the capillary zone, which leads to the criterion presented in equation (9). Equation (9) represents whether the given one-dimensional flow geometry has potential to disconnect. The initial value of  $h_c/(d + h_c)$  for our domain is 0.33, and equation (9) is fulfilled by our choice of initial  $K_{sc}$  and  $K_{sa}$  values.

The rates of the water table drop were classified as losing-connected, losing-transitional, or losing-disconnected, based on the behavior of the no-biomass-growth case according to the following classification scheme and total head gradient through the aquifer ( $dH/dz_a$ ) measured between the base of the



clogging layer and the groundwater level represented by a pressure head = 0 m. These definitions are rather loose constraints, as there is no exact cutoff between them:

1. Losing-connected: when the baseline no-growth case fails to reach the maximum flux after the 160 day simulation, and remains sensitive to increases in the total head gradient. The column remains saturated for the baseline no-growth case ( $dH/dz_a \ll 1$ ).
2. Losing-transitional: when the baseline no-growth case approaches the maximum flux, but remains sensitive to increases in the total head gradient. The column shows a small, unsaturated zone developing, where pressures are below zero but not yet surpassing air-entry ( $0 < dH/dz_a < 1$ ).
3. Losing-disconnected: when the baseline no-growth case reaches a maximum flux, is insensitive to changes in the total head gradient, and shows localized UG conditions (measured between the base of the clogging layer and the groundwater level represented by a pressure head = 0 m). Losing-disconnected cases experience connected conditions first, transition, and finally disconnection ( $dH/dz_a \rightarrow 1$ ).

From each 160 day simulation representing 5 months of summer conditions when bioclogging is most relevant, we extracted the following variables of interest: peak flux, daily clogging layer conductivities ( $K_{sc,new}$ ), daily unsaturated aquifer conductivities at a point below the clogging layer ( $K_{ua}$ ), the updated clogging layer saturated thickness ( $h_{c,new}$ ) with pressure head  $\geq 0$  m, and  $dH/dz_a$  from the base of the clogging layer to the water table. We chose this measurement strategy for  $dH/dz_a$  for two reasons: (1) measuring the hydraulic gradient in the unsaturated zone between the base of the clogging layer and the top of the capillary zone, for example, can show localized UG conditions well before maximum flux is reached, and (2) the total head gradient is not uniform throughout the one-dimensional domain. An elongated capillary zone has a total head gradient much smaller than that in the unsaturated zone where UG conditions are found. Combined with conductivities below air-entry, the capillary zone has the potential to be the flux-limiting zone. Our method provides a depth-integrated assessment of  $dH/dz_a$  values at the time of peak flux without assuming UG conditions a priori.

### 3.4. Effective Disconnection and Peak Flux

Disconnection and UG conditions may not always coincide with maximum seepage. Maximum infiltration has been shown to sometimes occur in the transition period leading up to full disconnection [Brunner *et al.*, 2009b; Rivière *et al.*, 2014]. We chose peak flux as the key variable of interest, because it represents the point at which the system transitions from flow defined by the time-dependency of the hydraulic gradient to flow defined by the time-dependency of hydraulic conductivity, as pointed out previously by Rivière *et al.* [2014]. We propose the term ‘effective disconnection,’ hereafter  $D-E_{ff}$ , to define these conditions occurring at peak flux, and to guide our interpretation of peak flux relative to the measurement of  $dH/dz_a$ . Effective disconnection is not characterized by the existence of UG conditions, but by the occurrence of peak flow. Additionally, we do not assume a priori that max flux may *only* occur for  $dH/dz_a$  values of 1; therefore,  $D-E_{ff}$  helps to define the occurrence of max fluxes at many values of  $dH/dz_a$  that occur during non-UG flow conditions. This implies that UG conditions are only required as an indicator of disconnection in the absence of biomass growth. Since we also measure changes in  $h_{c,new}$  over time, we explore how the criterion in equation (9) evolves from a static criterion to a dynamic one relative to changes in  $K_{sc}$  as the system desaturates.

### 3.5. Limitations to the One-Dimensional Approach

The one-dimensional modeling approach presents conceptual limitations to our river-aquifer flow system. A one-dimensional approach cannot capture complex spatial variability from river geometry or a two-dimensional groundwater mound. Larger scale features may govern flow paths and lead to situations where the river is connected in some areas (thalweg), and disconnected in others (bank), leading to preferential flow paths. A two-dimensional or three-dimensional model would be needed for these joint, spatiotemporal processes. Given that the flow direction is predominantly vertical, and since bioclogging can occur in many locations with a high nutrient flux, the overall trend of disconnection and bioclogging experienced by a point on the bank may be similar to other points in the near vicinity along the bank, or in other predominantly losing rivers. Additionally, our model does not account for other processes that would be required to replicate spatial and temporal variability of infiltration at all sites at daily timescales within the river, such as sediment deposition events, erosion/scour, mechanical clogging by the algal mat, transient river flow regimes, as well as temperature effects that influence water viscosity and biological growth rates. While our approach is not able to simulate total flow

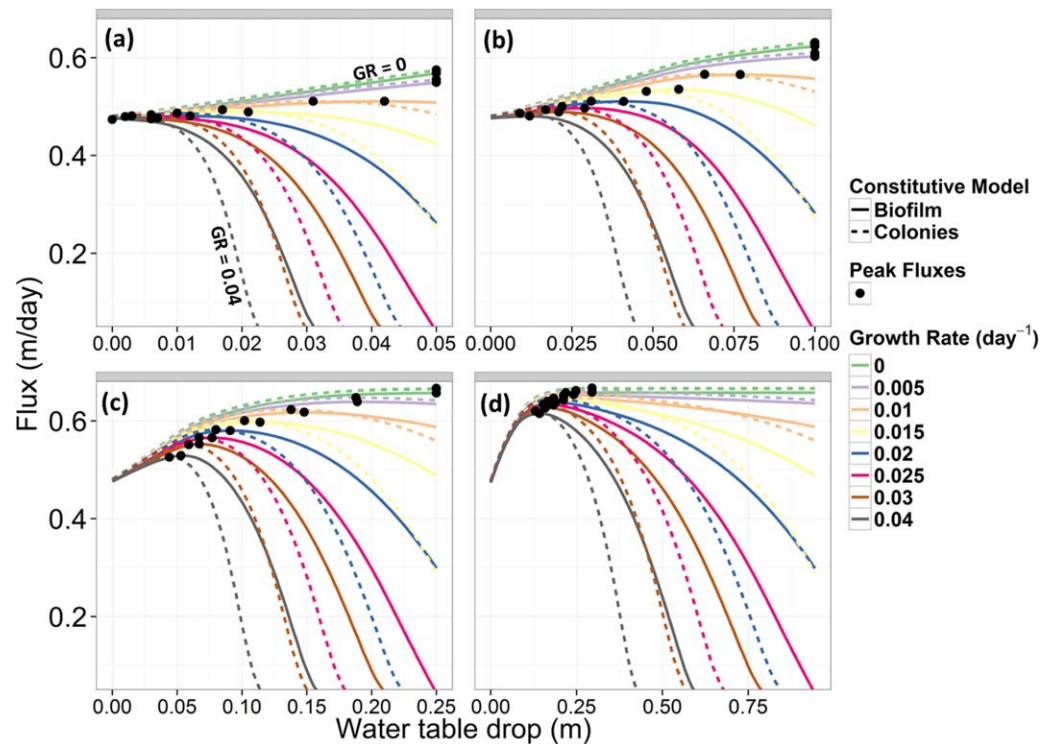


**Figure 4.** Seepage curves are shown as a function of the water table drop for a range of biomass growth rates (GR) and a range of water table decline rates. (a) Losing-connected:  $0.0313 \text{ cm d}^{-1}$ . (b) Losing-transitional:  $0.0625 \text{ cm d}^{-1}$ . (c) Losing-disconnected:  $0.1563 \text{ cm d}^{-1}$ . (d) Losing-disconnected:  $0.5900 \text{ cm d}^{-1}$ . The amount of time represented is the same for each simulation (160 days). Note the different scales for the x axis, which represent overall differences in the total water table drop over the 160 day simulation. The continuum of GR is the same for all plots. For interpretation of the color in all figure legends, the reader is referred to the web version of this article.

volumes to the RBF wells and joint spatial-temporal variability, it is sufficient to demonstrate our hypothesis along a vertical flow path at monthly to seasonal timescales.

## 4. Results

### 4.1. Biological Effects on Seepage

Seepage curves from the one-dimensional synthetic case study are shown across a range of water decline rates, considering conditions of a losing-connected river (Figure 4a), a losing-transitional river (Figure 4b), and a losing-disconnected river (Figures 4c and 4d), all coupled with permeability dynamics from biomass (represented as  $K_{SC, new}$  values in the modeling framework). The models illustrate that seepage follows the characteristic disconnection curve sequence (top solid green line for growth rate = 0, no-growth baseline case), and represents the synthetic case where no biomass grows and full disconnection is reached (Figures 4c and 4d). In all cases with biomass growth, seepage deviates substantially from the no-growth baseline scenario, and flux values never reach the same magnitude as the no-biomass-growth case. Figure 4 shows infiltration for both the Biofilm and Colonies models. Since results do not significantly vary between constitutive models, we only present results for the Colonies model in subsequent figures.

Peak fluxes depend on whether the river is losing-connected, losing-transitional, or losing-disconnected. For cases with slow water table drops (representing weak losing-connected conditions from slow pumping in Figure 4a), peak fluxes only exist at or near the beginning of the simulation. In the case of the highest biomass growth rate (GR) ( $0.04 \text{ day}^{-1}$ ), and the slowest water table drop (Figure 4a, grey curve), flux goes into decline and never reaches a peak. Losing-disconnected cases occur with the fastest water table drops (highest pumping, Figures 4c and 4d). As permeability declines (and biomass grows) simultaneously with lowering water tables, seepage does not immediately decline, but continues to increase. Seepage increases during the connected stage (where  $dH/dz_a \ll 1$ , but rising fast), and continues to increase until peak flux and  $D-E_{ff}$  is reached. Peak fluxes (black solid dots in all figures) are higher, occur earlier on in the fast water

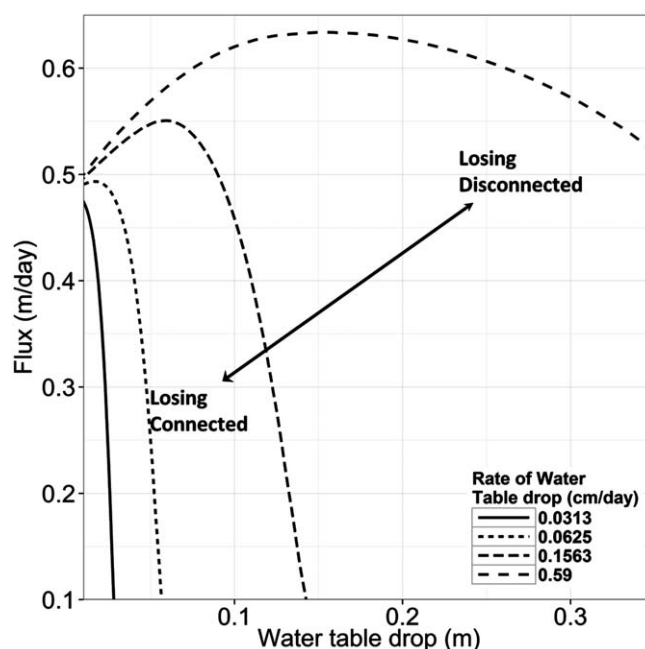


**Figure 5.** Infiltration fluxes with the Colonies model are shown as a function of the water table drop for a range of water table decline rates, for the moderate growth rate of 0.02 day, and an aquifer conductivity value of 100 m d<sup>-1</sup>. Slow water table drops represent cases that are losing-connected; fast water table drops represent losing-disconnected cases.

tirety of the simulation (Figure 5, green curves), will only show maximum seepage at the onset of the simulation if biomass grows fast and the gradient is not sufficient to pull flow. Peak flux is rarely achieved in losing-connected cases, because higher rates of water table drop are needed to overcome and outpace conductivity declines such that infiltration can be maintained or increased. Compared with a losing-disconnected river (Figure 5, yellow curve, dashed curve), the fast water table drop can help keep infiltration rates high at the beginning when biomass has not yet reached a volume sufficient for fully clogging the pore-space. Modeled fluxes follow a similar trend to those measured in the field, providing assurance that the two hypothesized processes are well represented (Figure 2, red line).

#### 4.2. Biological Effects on Pressure Head Profiles

Pressure head profile snapshots with depth under losing-connected and losing-disconnected conditions are shown in Figure 6 for day 90 (midway through the summer; Figures 6a and 6c), and the day of peak flux (day of peak flux varies by simulation; Figures 6b and 6d). Peak flux is typically reached midway through each simulation (between day 20 and 50). Unsaturated zone conditions present at the time of peak flux vary across the simulations. When comparing snapshots for the day of peak flux (Figures 6b and 6d), peak flux occurs without the presence of an unsaturated zone for the losing-connected case (Figure 6b), in contrast to the losing-disconnected case (Figure 6d), which shows peak flux occurring with the downward shift of the capillary zone. In the losing-disconnected case (Figure 6d) for a GR = 0, the zone where unit-gradient (UG) conditions are found and the zone where non-UG conditions are found is highlighted and demonstrate that our measurement strategy for  $dH/dz_a$  captures the linear and nonlinear conditions for  $dH/dz_a$ . While peak fluxes for biomass GR = 0 may coincide with localized UG conditions, depth-integrated  $dH/dz_a$  is not 1. Furthermore, for larger biomass GR, peak flux actually occurs with smaller capillary zones and non-UG conditions in the majority of the vertical domain.

For both cases of losing-connected and losing-disconnected rivers, peak flows are achieved when both pressure reduction from biomass growth (Figures 6c and 6d) and the rate of change of the hydraulic gradient are not enough to outpace the rate of change of conductivity. These two simultaneous and opposing processes dominate infiltration at different times, and only when the magnitude of one (clogging) outpaces

table decline cases, and show that water tables can drop a greater distance vertically before reaching peak flux compared to the losing-connected and losing-transitional cases. Even with the presence of biomass growth, seepage increases in strongly-losing rivers as a consequence of increasing total head gradients from the water table drop and from the decline in the pressure head at the base of the clogging layer.

Infiltration fluxes are compared as a function of the water table drop in Figure 5 for a range of water table decline rates for the moderate GR of 0.02 day, and an aquifer conductivity value of 100 m d<sup>-1</sup>. Slow water table drops represent cases that are classified as losing-connected, because under no-biomass-growth scenarios they never produce an unsaturated zone. A river that is weakly losing, and remains losing-connected for the en-

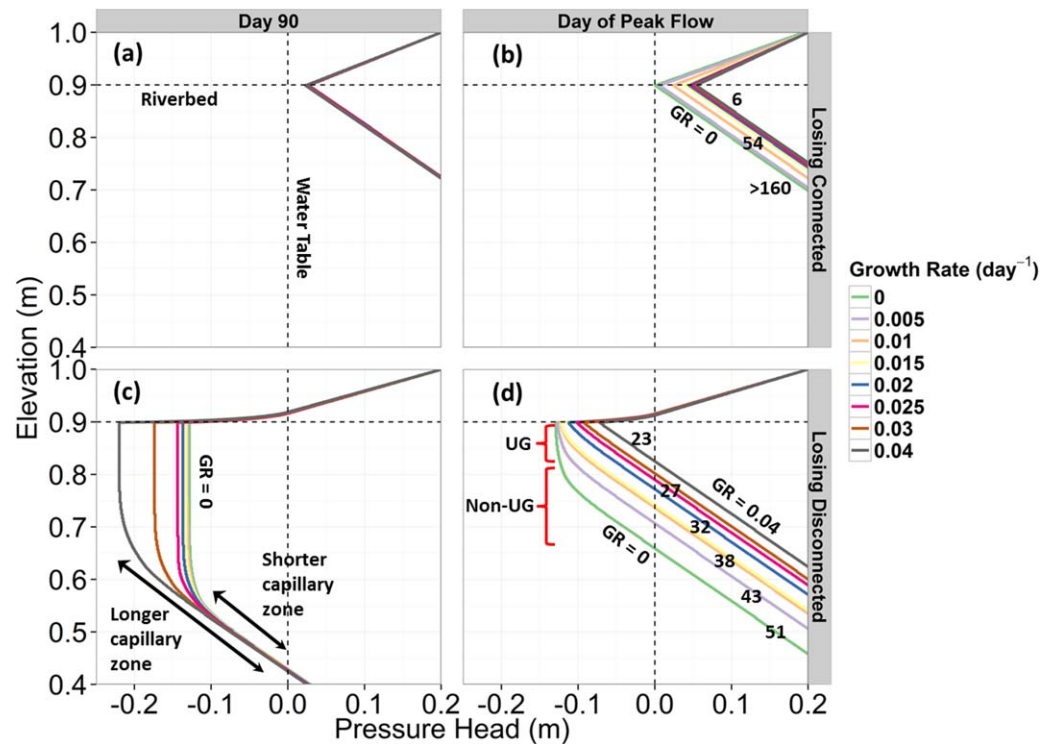


**Figure 6.** Pressure head profiles with depth for losing-connected and losing-disconnected conditions. Different snapshots in time are shown representing day 90 ((a) and (c) midway through the summer), and (b) and (d) snapshots on the day of the simulation when peak flux occurred). A few time stamps for peak fluxes are shown on top of each line. For the losing-disconnected case, on day 90 the water table is found at 0.42 m elevation, which represents a total water table drop of 0.53 m from the starting position of 0.95 m. Unit-gradient (UG) and non-UG zones are pointed out for GR = 0.

the other (increases in gradient), does peak flux occur which we define as the point of ‘effective disconnection,’  $D-E_{ff}$ . In all scenarios, peak flux occurs when  $D-E_{ff}$  is reached with  $dH/dz_a < 1$ .

When comparing unsaturated zone conditions on the same day (Day 90; Figures 6a, c), it is clear that biomass growth affects unsaturated zone conditions by reducing (more negative) the pressure at the bottom of the clogging layer, and extending the length of the capillary zone in the aquifer and clogging layer (Figure 6c). For the losing-disconnected case (6c), higher rates of biomass growth show noticeable drops in pressure beneath the clogging layer, leading to longer and more tension-dominated capillary zones compared with low biomass growth rates and losing-connected conditions. UG conditions above the capillary zone are visible in Day 90 for all GR. Yet  $dH/dz_a$  conditions vary because of capillary zone length (Figure 6c). The inverted water table is also noticeable in these simulations leading to a smaller extent of saturation ( $h_{c,new}$ ) within the clogging layer.

Figure 7 shows pressure heads measured at the base of the clogging layer (elevation = 0.9 m), conductivity as a function of bioclogging, and total head gradients ( $dH/dz_a$ ) measured between the base of the clogging layer and the water table represented by a pressure head equal to 0 m. The point in time at which peak flux occurs is shown by the black dots (same peak fluxes from Figure 4), and represents  $D-E_{ff}$ . As  $dH/dz_a$  increases, the pressure head approaches a minimum (Figure 7a). Large biomass GR shift  $dH/dz_a$  toward smaller values of the water table drop at the time of  $D-E_{ff}$ , and hence hasten the onset of  $D-E_{ff}$  (Figure 7c). This is consistent with Figure 6d, where the length of the unsaturated zone is smaller at the onset of  $D-E_{ff}$  for higher biomass GR. Take note of the green curve in Figure 7c, which is the case with no biomass growth. For this case, peak flux occurs when  $dH/dz_a \approx 0.5$ . Our measurement strategy that “follows the water table” was chosen to account for the effects of the transition phase and the lengthened capillary zone (Figure 6c). If the measurement of  $dH/dz_a$  was taken at two static points, one at the base of the clogging layer and another at a point 10 cm below the clogging layer,  $dH/dz_a$  would be 1 much earlier. However, this would overlook the effects of a growing capillary zone on flow through the entire 1 m domain (see Figure 6d for the localized zone of UG conditions at peak flux for the GR=0 case only).

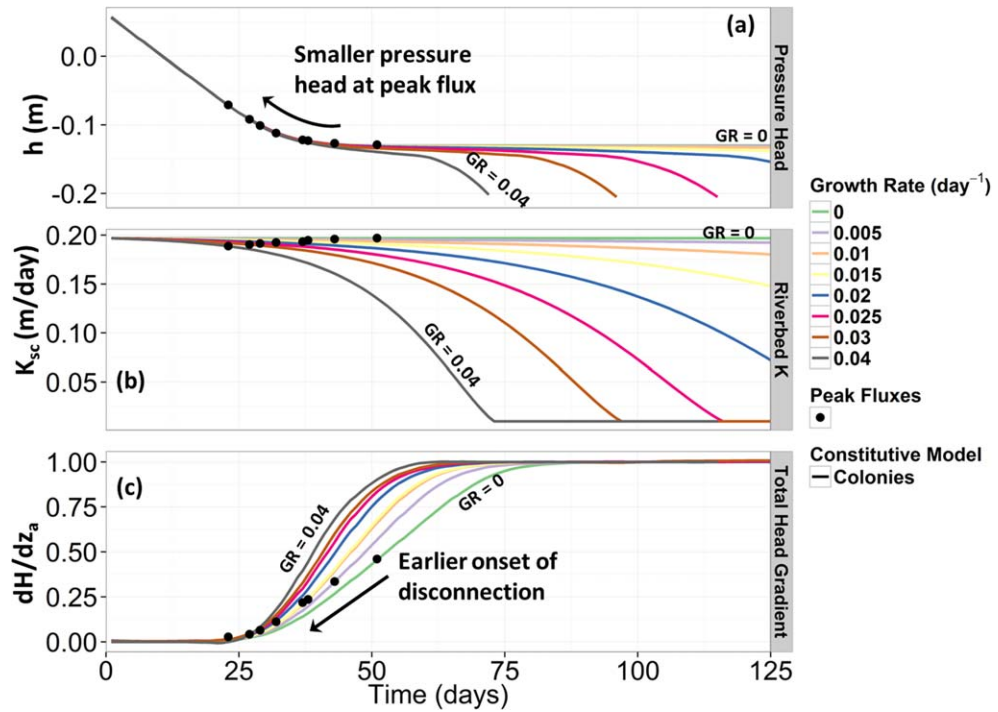


**Figure 7.** (a) Pressure heads measured at the base of the clogging layer. (b) Conductivity declines in the riverbed layer from bioclogging. (c)  $dH/dz_a$  shown as functions of time for different values of the biomass growth rate and the Colonies model. As the total head gradient increases, the pressure head approaches a minimum. The point in time at which peak flux occurs is shown by the black dots.

#### 4.3. An Effective Disconnection Criterion

Using the extracted variables of interest during peak flux ( $K_{sc, new}$ ,  $K_{ua}$ ,  $dH/dz_a$ ,  $h_{c, new}$ , with peak flux represented as the dots in Figure 4), we deduce two different states of the system depending on the biomass GR. A visualization of these two states is shown in Figure 8. We plotted the ratio of the updated conductivities ( $K_{sc, new}/K_{ua}$ ) against  $dH/dz_a$ , and the disconnection criterion from equation (9) against  $dH/dz_a$ . For large rates of biomass growth (Figure 8, linear model), peak flux occurs when:

$$\frac{K_{sc, new}}{K_{ua}} \approx \frac{dH}{dz_a} \quad (10)$$

This criterion shown by the fitted model in Figure 8 defines the point when effective disconnection occurs and displays a significant modification to the static disconnection criteria defined in equation (9).

For small rates of biomass growth, peak flux occurs at larger values of  $dH/dz_a$  (Figure 8, asymptote) coincident with larger capillary zones and an inverted water table in the clogging layer (represented by changes in  $h_{c, new}$ ). In the cases where no biomass grows, peak flux occurs when  $K_{sc, new}/K_{ua}$  reaches the inflection point of the  $dH/dz_a$  curve (Figure 7b). Specifically, peak flux for low/no biomass growth cases approximates a dynamic disconnection criterion:

$$\frac{K_{sc, new}}{K_{ua}} \approx \frac{h_{c, new}}{d + h_{c, new}} \quad (11)$$

The two states shown in Figure 8 represent a distinction between cases when  $D-E_{ff}$  occurs *before* the unsaturated zone and inverted water table develop (high rates of biomass growth—fast permeability declines), and cases *after* these features develop (low rates of biomass growth—slow permeability declines). In all cases, peak flux occurs at the point of  $D-E_{ff}$  between fully connected and disconnected flow and when  $dH/dz_a < 1$ . As the GR approaches 0, the pressure profiles exhibit localized UG conditions and get closer to the dynamic criteria from equation (9). Some of the points for GR=0 do not fall on the evolving criteria line because of very slow pumping rates reaching 160 days without significant unsaturated zone growth.



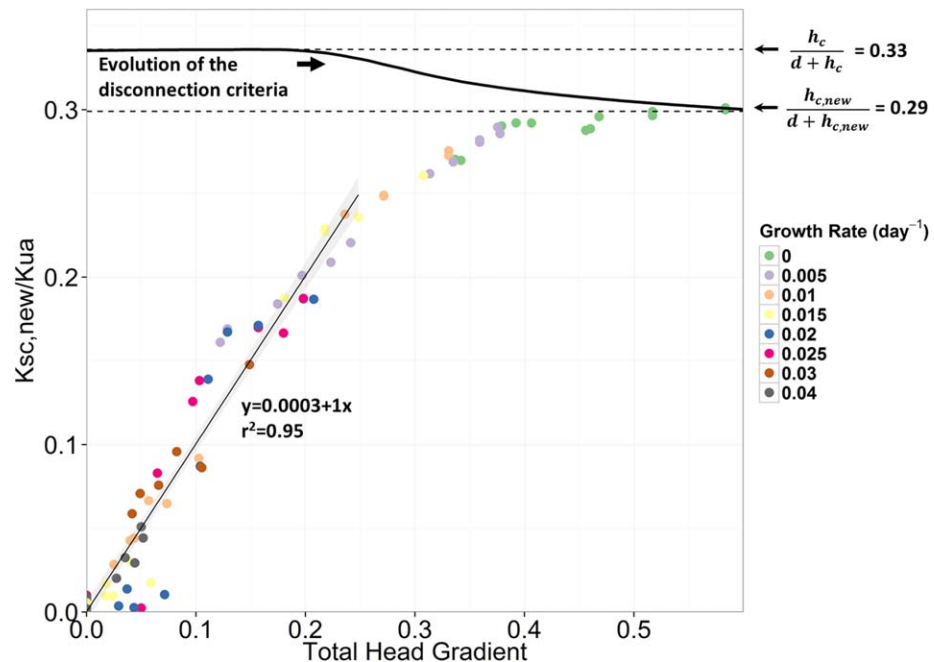


**Figure 8.** Ratio  $K_{sc,new}/K_{ua}$  plotted against  $dH/dz_a$  across the range of biomass growth rates, and rates of water table drop, measured at the time of peak flux. The dashed lines in Figure 8 represent the bounds of the disconnection criterion (equation (9)). The solid black line is the evolution of the criterion as the water table declines and an inverted water table forms in the clogging layer beginning at 0.33 and evolving to 0.29. The bounds represents cases with low biomass growth rates, and shows the asymptote of  $K_{sc,new}/K_{ua}$  as it approaches the updated disconnection criterion. The linear model represents cases with fast biomass growth rates, and shows the linear one-to-one relation between  $K_{sc,new}/K_{ua}$  and  $dH/dz_a$  at the point of peak flux. Green dots show the baseline no-growth case. The green dots should be overlapping, and exactly equal. However, in many scenarios the simulation finished before full disconnection was reached (e.g., in the losing-connected cases), and thus shows lower total head gradient for the peak, marking the end of the simulation.

For large biomass GR, peak fluxes occur when  $K_{sc,new}/K_{ua}$  is approximately  $dH/dz_a$  (equation (10)). Peak fluxes tend to occur earlier, typically while the system is still completely saturated (Figures 6b and 6d). In the high GR cases, the ratio  $K_{sc,new}/K_{ua}$  diverges from the disconnection criterion because peak flux occurs with small values of  $dH/dz_a$ . In these cases the unsaturated zone and inverted water table are not fully developed, as the capillary zone is still in contact with the clogging layer. Large biomass growth rates change the ratio of  $K_{sc,new}/K_{ua}$  faster than changes to  $dH/dz_a$ , because  $K_{ua}$  is still relatively large compared with  $K_{sc,new}$ . When these two ratios are equal, peak flux is reached.

For small biomass GR, peak flux does not occur until a capillary zone, an unsaturated zone, and an inverted water table are almost fully developed (Figure 8, Evolution of the disconnection criteria). In the cases where no biomass grows, as the unsaturated zone develops, peak flux occurs when  $K_{sc,new}/K_{ua}$  converges to the updated, dynamic disconnection criterion (equation (10)). Biomass produces negligible pressure declines at the base of the clogging layer and  $K_{sc,new}$  does not decline fast enough, thus allowing  $dH/dz_a$  to be larger at the onset of peak flux.

## 5. Discussion

### 5.1. Bioclogging Effects on Seepage

The synthetic case study demonstrated that dynamic permeability and connection status must be accounted for to accurately simulate infiltration trends. Biomass growth reduced seepage by reducing the hydraulic conductivity; however the importance of this depends on whether the baseline case for the river is losing-connected or losing-disconnected, and the strength of losing conditions. For strongly losing rivers (Figures 4c and 4d), seepage continued to grow even while  $K_{sc}$  declined and showed peak flux once  $D-E_{ff}$  was reached. It is during these early stages that field observations may show simultaneous seepage increases and hydraulic conductivity decreases, which can typically confound system interpretation and



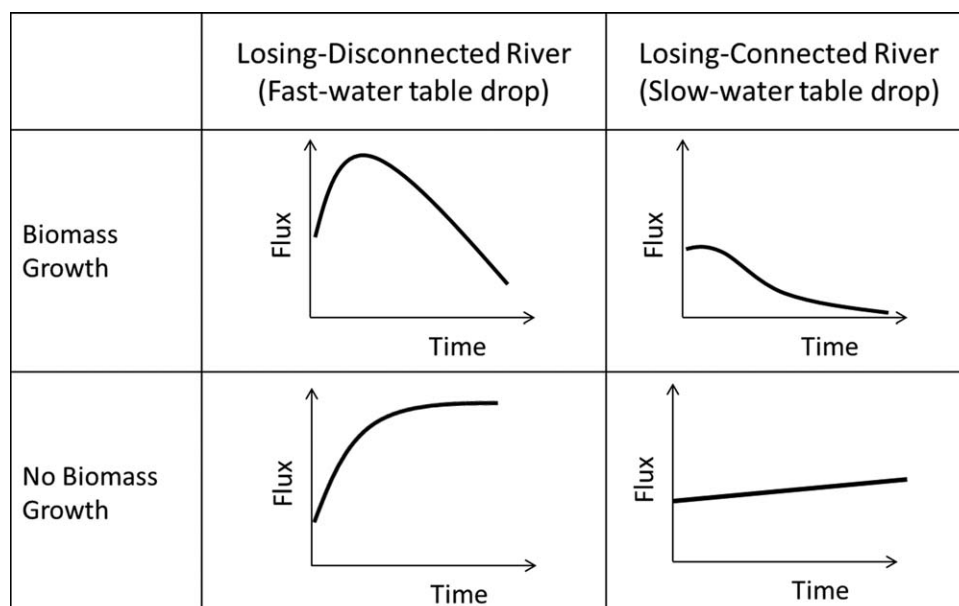


**Figure 9.** Generalized trends for infiltration in a losing river when experiencing biomass growth, as well as strong or weak losing conditions.

model development. Increasing the rate of the water table drop (such as through higher pumping rates) will result in greater infiltration rates, but consequently a larger unsaturated zone during peak seepage (Figures 6b and 6d), and quicker declines postdisconnection. In weak losing-connected reaches, where hydraulic gradients remain small (Figures 4a, 5, and 6b), the pressure decline from biomass growth, as well as the limited  $dH/dz_a$  increases, is not large enough to overcome the conductivity decline, resulting only in seepage decreases. With no biomass growth, weak losing rivers are only able to show slight infiltration increases. Figure 9 shows a generalized schematic of the nature of these dual processes and the overall effects on infiltration.

In a river undergoing disconnection, this behavior indicates that infiltration is highly sensitive to riverbed permeability changes only after  $D-E_{ff}$  is reached. For strongly losing rivers and high rates of biomass growth,  $D-E_{ff}$  occurs much earlier than UG conditions (Figure 7b). In a river remaining connected, the behavior of the peak flux and the apparent insensitivity to water table declines while still fully saturated indicate that  $D-E_{ff}$  occurs without the presence of an unsaturated zone. In the case of losing-connected rivers that experience clogging, that insensitivity occurs earlier than in losing-disconnected rivers. In terms of practical RBF management, increasing pumping early in the summer before conditions become favorable for biomass growth may lead to disconnection, and thus increased total production volumes compared to maintaining the river at losing-connected conditions. Such strategies could also be beneficial for optimizing other water management practices, such as bank storage and managed aquifer recharge.

Several processes that may influence infiltration were not considered in this study. In our simulations, we did not introduce feedback effects from declining infiltration and nutrient fluxes on biomass growth, because the goal of our simulations was only to test field observed biomass growth as a constraint on infiltration trends. When a river is undergoing disconnection, infiltration can change the nutrient flux entering the riverbed, which can potentially drive or inhibit biomass growth. Where pumping drives bioclogging through increased fluxes, feedback effects between clogging and pumping would need consideration. It is unknown how cycling pumping will change overall microbial growth. We also did not test the effects of water table fluctuations and/or effects of accelerating water table declines on infiltration. Other processes not considered here, but potentially relevant for site specific infiltration prediction at daily time scales, include: scouring and sediment disturbance events (which have been shown to increase infiltration by a factor of 7 [Rosenberry et al., 2010]), transient river flow boundaries, mechanical clogging from algal growth, grazer-algal food chain dynamics [Power et al., 2008], preferential flow paths, river geometry, and parameter sensitivity to temperature. All of these processes might also contribute to the dynamics of the infiltration

rates. However, our results show that even in the absence of these processes, seasonal changes of infiltration rates can be explained through observations of bioclogging and disconnection.

## 5.2. Importance of the Transition Phase

The transition phase represents the time where  $dH/dz_a$  is changing fast, and flow becomes dominated by conductivity declines. This phase was shown to occur differently based on biomass growth conditions. We found peak fluxes occurred during the transition phase precisely when reaching  $D-E_{ff}$ .

When there is a permeability and porosity reduction from biomass growth, physically the pore space is reduced, and pressure head values decline (become more negative) (Figures 6c and 7a). The drop in the pore space pressure at the clogging layer-aquifer interface increases the hydraulic gradient while simultaneously reducing  $K_{ua}$ . These processes act in opposition until the  $D-E_{ff}$ , when peak flux occurs, at which time the conductivity drops become the dominating process. For fast biomass growth rates, the resulting  $K_{sc,new}/K_{ua}$  ratio occurs when total head gradients are  $\ll 1$  and biomass growth works to hasten the onset of  $D-E_{ff}$  (Figure 7b).

In the literature, full disconnection is approximated as either  $dH/dz_a \sim 1$ , or when total head gradients no longer affect the infiltration rate [Brunner *et al.*, 2011]. In this work we measured  $dH/dz_a$  between a point directly below the clogging layer and the water table. Using this depth-integrated approach, we found that effective disconnection occurred for the no-biomass growth case when  $dH/dz_a \sim 0.5$ , which is the inflection point of the  $dH/dz_a$  curve, and during the transition phase (Figure 7c, green curve). This is in line with previous interpretations of peak flux representing a shift from changes in flow dominated by gradient to changes in flow dominated by conductivity declines [Rivière *et al.*, 2014]. With biomass growth, this point of effective disconnection occurs much earlier in time (Figure 7c), and precisely occurs at the time when head changes become negligible compared to conductivity changes (Figure 8).

The transition phase is important because it pinpoints the time when water managers should monitor water tables and pumping to account for bioclogging impacts. After the transition phase, any increase in pumping will have negligible effects on infiltration from the river. In most cases, the portion of water infiltrated by the additional pumping will increasingly draw from the alluvial aquifer, or additional sections of the river such as the thalweg undergoing disconnection from the larger radial extent of the cone of depression. Only when water tables are already low will the impact of biomass and disconnection negatively affect pumping.

## 5.3. Predicting Peak Flux From Effective Disconnection

In all cases of biomass growth, simulated flux does not begin to decline until  $D-E_{ff}$  is reached. In the losing-connected case,  $D-E_{ff}$  occurs without the existence of an unsaturated zone (below air-entry). In some of the losing-connected cases, flux increases due to gains in the hydraulic gradient. However, the flow becomes "effectively disconnected," in the sense that water tables declines can no longer drive flow. In fact, even in the fully connected cases where no unsaturated zone develops, permeability declines are much more dominant in determining the magnitude of flux, because they are orders of magnitude greater than water table declines. In all simulations, peak fluxes and  $D-E_{ff}$  are occurring before  $dH/dz_a = 1$ . This result is in agreement with Brunner *et al.* [2010] and Rivière *et al.* [2014], who showed peak fluxes occurred during the transition phase rather than during disconnection. Our 'follow the water table' measurement strategy for  $dH/dz_a$  shows that  $D-E_{ff}$  occurs for two different states of the system, depending on whether biomass GR are large or small relative to water table drop rates.  $D-E_{ff}$  can be used to predict when peak fluxes occur given measurements of subsurface conditions of  $dH/dz_a$ . Since pressure conditions below the riverbed are mostly unknown without direct measurements, water managers may find it beneficial to install piezometers directly below the riverbed to monitor the extent of disconnection, and decide to bank more water as subsurface storage before infiltration rates decline.

## 6. Summary and Conclusions

In this study, we systematically investigated (1) how permeability dynamics induced through bioclogging affect the exchange of flows between a river and its underlying aquifer as a function of the connection status of the river, (2) established a  $D-E_{ff}$  criterion for predicting when peak fluxes occur relative to pressure head and total head gradient conditions in the subsurface, and (3) developed simple numerical capabilities that permit exploration and predictive understanding of coupled field-scale processes. We tested the net

effect of two opposing phenomena: (1) the drop of water table leading to increased fluxes, and (2) bioclogging leading to decreased fluxes. For each case, we considered different rates of changes, and examined how net fluxes depend on combinations of the differing rates of change, and on the existence and timing of peak flux.

Our study highlights that consideration of riverbed dynamic permeability coupled with the connection status of the river is required for accurate prediction of infiltration dynamics. We found that bioclogging ultimately controls the magnitude of the infiltration flux. However, the process of disconnection relative to permeability changes governs the timing of peak flux (Figure 7) and unsaturated zone growth (Figure 6). Characteristic seepage curves of coupled biomass growth, combined with scenarios of losing-connected and losing-disconnected rivers, highlight a dynamic, dual influence on infiltration (Figure 9).

Our research provides an explanation of the processes occurring in natural rivers that can explain field measurements that show simultaneous permeability declines and seepage increases. Diverging trends in temporally dynamic permeability and seepage can indicate a river is undergoing disconnection simultaneously with biomass growth, and this research explains the nature of their dual influence. In this work we also explored the criteria for  $D-E_{ff}$  as a predictor of peak fluxes, which always occurred during the transition phase when head changes became negligible compared to conductivity changes. Our work presents the idea of 'effective disconnection' to account for unsaturated zone growth and dynamic permeability.

Better understanding the mechanisms controlling riverbed clogging and its impacts on groundwater-surface water interactions can provide quantitative protocols for managing pumping. These prediction methods can also inform assessments of biological factors in managing RBF systems. Future work needs to incorporate streambed morphology and texture, feedbacks between infiltration and bioclogging which can limit and enhance biological growth, and nutrient limitations on growth, and account for infiltration differences in gaining and losing rivers showing various degrees of dynamic permeability. At even larger scales (e.g., catchment-scales), it is not yet understood how biomass growth in the entire river corridor may affect regional water balances, hyporheic flows, and river discharge, especially in drought-prone climates. Recognition of the feedbacks of bioclogging at different geomorphological and hydrological scales can lead to better estimates of local water volumes and pumping capacities, especially when these systems are used as municipal and public water supply sources.

## Acknowledgments

This research was supported by the Jane Lewis Fellowship from the University of California, Berkeley, the Sonoma County Water Agency (SCWA), the Roy G. Post Foundation Scholarship, the U.S. Department of Energy, Office of Science, Office of Biological and Environmental Research under award DE-AC02-05CH11231, and the UFZ-Helmholtz Centre for Environmental Research, Leipzig, Germany. We thank Marcus Trotta, Donald Seymour, John Mendoza, and Jay Jasperse of SCWA for their useful suggestions. We would also like to acknowledge the efforts of Markus Neubauer, Gerrit Laube, Falk Heße, Changhong Wang, Brad Harken, Heather Savoy, Karina Cucchi, Jon Sege, and the anonymous reviewers for their helpful comments and ideas. Supporting information can be found in the online version of this article.

## References

- Alarcon, V. J., D. Johnson, W. H. McAnally, J. van der Zwaag, D. Irby, and J. Cartwright (2014), Nested hydrodynamic modeling of a coastal river applying dynamic-coupling, *Water Resour. Manage.*, 28(10), 3227–3240, doi:10.1007/s11269-014-0671-6.
- Annan, J. D. (2001), Modelling under uncertainty: Monte Carlo methods for temporally varying parameters, *Ecol. Modell.*, 136(2–3), 297–302, doi:10.1016/S0304-3800(00)00413-0.
- Barahona-Palomo, M., M. Riva, X. Sanchez-Vila, E. Vazquez-Sune, and A. Guadagnini (2011), Quantitative comparison of impeller-flowmeter and particle-size-distribution techniques for the characterization of hydraulic conductivity variability, *Hydrogeol. J.*, 19(3), 603–612, doi:10.1007/s10040-011-0706-5.
- Battin, T. J., and D. Sengschmitt (1999), Linking sediment biofilms, hydrodynamics, and river bed clogging: Evidence from a large river, *Microb. Ecol.*, 37(3), 185–196, doi:10.1007/s002489900142.
- Baveye, P., P. Vandevivere, B. L. Hoyle, P. C. DeLeo, and D. S. de Lozada (1998), Environmental impact and mechanisms of the biological clogging of saturated soils and aquifer materials, *Crit. Rev. Environ. Sci. Technol.*, 28(2), 123–191, doi:10.1080/1064338981254197.
- Blaschke, A. P., K.-H. Steiner, R. Schmalfluss, D. Gutknecht, and D. Sengschmitt (2003), Clogging processes in hyporheic interstices of an impounded river, the Danube at Vienna, Austria, *Int. Rev. Hydrobiol.*, 88(3–4), 397–413, doi:10.1002/iroh.200390034.
- Brovelli, A., F. Malaguerra, and D. A. Barry (2009), Bioclogging in porous media: Model development and sensitivity to initial conditions, *Environ. Model. Software*, 24(5), 611–626, doi:10.1016/j.envsoft.2008.10.001.
- Brown, K., and A. Wherrett (2014), Fact sheets bulk density-measurement, *Soil Qual.* [Available at <http://soilquality.org.au/factsheets/bulk-density-measurement>], last accessed 15 Sept 2014.]
- Brun, A., and P. Engesgaard (2002), Modelling of transport and biogeochemical processes in pollution plumes: Literature review and model development, *J. Hydrol.*, 256(3–4), 211–227, doi:10.1016/S0022-1694(01)00547-9.
- Brunner, P., P. G. Cook, and C. T. Simmons (2009a), Hydrogeologic controls on disconnection between surface water and groundwater, *Water Resour. Res.*, 45, W01422, doi:10.1029/2008WR006953.
- Brunner, P., C. T. Simmons, and P. G. Cook (2009b), Spatial and temporal aspects of the transition from connection to disconnection between rivers, lakes and groundwater, *J. Hydrol.*, 376(1–2), 159–169, doi:10.1016/j.jhydrol.2009.07.023.
- Brunner, P., C. T. Simmons, P. G. Cook, and R. Therrien (2010), Modeling surface water-groundwater interaction with MODFLOW: Some considerations, *Ground Water*, 48(2), 174–180, doi:10.1111/j.1745-6584.2009.00644.x.
- Brunner, P., P. G. Cook, and C. T. Simmons (2011), Disconnected surface water and groundwater: From theory to practice, *Ground Water*, 49(4), 460–467, doi:10.1111/j.1745-6584.2010.00752.x.
- Coughlan, K., H. Cresswell, and N. McKenzie (2002), *Soil Physical Measurement and Interpretation for Land Evaluation*, CSIRO Land and Water Aust. Soil and Land Surv. Handb. Ser., 5, 35–58.

- Crosbie, R. S., A. R. Taylor, A. C. Davis, S. Lamontagne, and T. Munday (2014), Evaluation of infiltration from losing-disconnected rivers using a geophysical characterisation of the riverbed and a simplified infiltration model, *J. Hydrol.*, **508**, 102–113, doi:10.1016/j.jhydrol.2013.07.045.
- Dillon, P. J., and J. A. Liggett (1983), An ephemeral stream-aquifer interaction model, *Water Resour. Res.*, **19**(3), 621–626, doi:10.1029/WR019i003p00621.
- Doppler, T., H.-J. H. Franssen, H.-P. Kaiser, U. Kuhlman, and F. Stauffer (2007), Field evidence of a dynamic leakage coefficient for modelling river-aquifer interactions, *J. Hydrol.*, **347**(1–2), 177–187, doi:10.1016/j.jhydrol.2007.09.017.
- Dupin, H. J., P. K. Kitanidis, and P. L. McCarty (2001), Pore-scale modeling of biological clogging due to aggregate expansion: A material mechanics approach, *Water Resour. Res.*, **37**(12), 2965–2979, doi:10.1029/2001WR000306.
- Engeler, I., H. J. Hendricks Franssen, R. Müller, and F. Stauffer (2011), The importance of coupled modelling of variably saturated groundwater flow-heat transport for assessing river-aquifer interactions, *J. Hydrol.*, **397**(3–4), 295–305, doi:10.1016/j.jhydrol.2010.12.007.
- Ezeuko, C. C., A. Sen, A. Grigoryan, and I. D. Gates (2011), Pore-network modeling of biofilm evolution in porous media, *Biotechnol. Bioeng.*, **108**(10), 2413–2423, doi:10.1002/bit.23183.
- Fox, G. A., and D. S. Durnford (2003), Unsaturated hyporheic zone flow in stream/aquifer conjunctive systems, *Adv. Water Resour.*, **26**(9), 989–1000, doi:10.1016/S0309-1708(03)00087-3.
- Genereux, D. P., S. Leahy, H. Mitasova, C. D. Kennedy, and D. R. Corbett (2008), Spatial and temporal variability of streambed hydraulic conductivity in West Bear Creek, North Carolina, USA, *J. Hydrol.*, **358**(3–4), 332–353, doi:10.1016/j.jhydrol.2008.06.017.
- Gupta, R. P., and D. Swartzendruber (1962), Flow-associated reduction in the hydraulic conductivity of quartz sand, *Soil Sci. Soc. Am. Proc.*, **26**(1), 6, doi:10.2136/sssaj1962.03615995002600010003x.
- Harding Lawson Associates (1988), *Hydrogeologic Investigation Wohler Aquifer Study*, Sonoma County, Calif.
- Harvey, J., and M. Gooseff (2015), River corridor science: Hydrologic exchange and ecological consequences from bedforms to basins, *Water Resour. Res.*, **51**, 6893–6922, doi:10.1002/2015WR017617.
- Hatch, C. E., A. T. Fisher, C. R. Ruehl, and G. Stemler (2010), Spatial and temporal variations in streambed hydraulic conductivity quantified with time-series thermal methods, *J. Hydrol.*, **389**(3–4), 276–288, doi:10.1016/j.jhydrol.2010.05.046.
- Internal Report Published online by Sonoma County Water Agency (SCWA). [Available at <http://www.scwa.ca.gov/files/docs/projects/MirabelFishScreenFishLadderRepl2013/GeoTech/12Wohler%20Aquifer%20Study.pdf>.]
- Jaramillo, M. (2012), Riverbank filtration: An efficient and economical drinking-water treatment technology, *DYNA*, **79**(171), 148–157.
- Kildsgaard, J., and P. Engesgaard (2001), Numerical analysis of biological clogging in two-dimensional sand box experiments, *J. Contam. Hydrol.*, **50**(3–4), 261–285, doi:10.1016/S0169-7722(01)00109-7.
- Kim, D.-S., S. Thomas, and H. S. Fogler (2000), Effects of pH and trace minerals on long-term starvation of leuconostoc mesenteroides, *Appl. Environ. Microbiol.*, **66**(3), 976–981, doi:10.1128/AEM.66.3.976-981.2000.
- Kurtz, W., H.-J. Hendricks Franssen, and H. Vereecken (2012), Identification of time-variant river bed properties with the ensemble Kalman filter, *Water Resour. Res.*, **48**, W10534, doi:10.1029/2011WR011743.
- Lamontagne, S., A. R. Taylor, R. S. Crosbie, and P. G. Cook (2011), Interconnection of surface and groundwater systems-river losses from losing/disconnected streams, Billabong Creek Site Report, in *Water for a Healthy Country Flagship Report Series*, 37 pp., NSW Office of Water, Wollie Creek, Australia.
- McCallum, A. M., M. S. Andersen, B. M. S. Giambastiani, B. F. J. Kelly, and R. Ian Acworth (2013), River-aquifer interactions in a semi-arid environment stressed by groundwater abstraction, *Hydrol. Processes*, **27**(7), 1072–1085, doi:10.1002/hyp.9229.
- Molz, F. J., M. A. Widdowson, and L. D. Benefield (1986), Simulation of microbial growth dynamics coupled to nutrient and oxygen transport in porous media, *Water Resour. Res.*, **22**(8), 1207–1216, doi:10.1029/WR022i008p01207.
- Murphy, E. M., and T. R. Ginn (2000), Modeling microbial processes in porous media, *Hydrogeol. J.*, **8**(1), 142–158.
- Or, D., S. Phutane, and A. Dechesne (2007), Extracellular polymeric substances affecting pore-scale hydrologic conditions for bacterial activity in unsaturated soils, *Vadose Zone J.*, **6**(2), 298–305, doi:10.2136/vzj2006.0080.
- PC-Progress (2011), *PC-PROGRESS - Homepage*, *PC-Progress Eng. Software Development*. [Available at <http://www.pc-progress.com/en/Default.aspx>, last accessed 13 Jan 2012.]
- Peterson, D. M. (1989), *Modeling the Effects of Variably Saturated Flow on Stream Losses*, Harding Lawson Assoc., Novato, Calif.
- Power, M. E., M. S. Parker, and W. E. Dietrich (2008), Seasonal reassembly of a river food web: Floods, droughts, and impacts of fish, *Ecol. Monogr.*, **78**(2), 263–282, doi:10.1890/06-0902.1.
- Rivière, A., J. Gonçalves, A. Jost, and M. Font (2014), Experimental and numerical assessment of transient stream-aquifer exchange during disconnection, *J. Hydrol.*, **517**, 574–583, doi:10.1016/j.jhydrol.2014.05.040.
- Rockhold, M. L., R. R. Yarwood, M. R. Niemet, P. J. Bottomley, and J. S. Selker (2002), Considerations for modeling bacterial-induced changes in hydraulic properties of variably saturated porous media, *Adv. Water Resour.*, **25**(5), 477–495, doi:10.1016/S0309-1708(02)00023-4.
- Rockhold, M. L., R. R. Yarwood, M. R. Niemet, P. J. Bottomley, and J. S. Selker (2005), Experimental observations and numerical modeling of coupled microbial and transport processes in variably saturated sand, *Vadose Zone J.*, **4**(2), 407, doi:10.2136/vzj2004.0087.
- Rosenberry, D. O., L. Toran, and J. E. Nyquist (2010), Effect of surficial disturbance on exchange between groundwater and surface water in nearshore margins, *Water Resour. Res.*, **46**, W06518, doi:10.1029/2009WR008755.
- Rosenzweig, R., A. Furman, C. Dosoretz, and U. Shavit (2014), Modeling biofilm dynamics and hydraulic properties in variably saturated soils using a channel network model, *Water Resour. Res.*, **50**, 5678–5697, doi:10.1002/2013WR015211.
- Samsó, R., J. García, P. Molle, and N. Forquet (2016), Modelling bioclogging in variably saturated porous media and the interactions between surface/subsurface flows: Application to constructed wetlands, *J. Environ. Manage.*, **165**, 271–279, doi:10.1016/j.jenvman.2015.09.045.
- Schaap, M. G., F. J. Leij, and M. T. van Genuchten (2001), Rosetta: A computer program for estimating soil hydraulic parameters with hierarchical pedotransfer functions, *J. Hydrol.*, **251**(3–4), 163–176, doi:10.1016/S0022-1694(01)00466-8.
- Seki, K., M. Thullner, J. Hanada, and T. Miyazaki (2006), Moderate Bioclogging Leading to Preferential Flow Paths in Biobarriers, *Ground Water Monit. Rem.*, **26**(3), 68–76, doi:10.1111/j.1745-6592.2006.00086.x.
- Simunek, J., M. T. van Genuchten, and M. Sejna (2008), Development and applications of the HYDRUS and STANMOD software packages and related codes, *Vadose Zone J.*, **7**(2), 587–600, doi:10.2136/vzj2007.0077.
- Soleimani, S., P. J. Van Geel, O. B. Isgor, and M. B. Mostafa (2009), Modeling of biological clogging in unsaturated porous media, *J. Contam. Hydrol.*, **106**(1–2), 39–50, doi:10.1016/j.jconhyd.2008.12.007.
- Su, G. W., J. Jasperse, D. Seymour, J. Constantz, and Q. Zhou (2007), Analysis of pumping-induced unsaturated regions beneath a perennial river, *Water Resour. Res.*, **43**, W08421, doi:10.1029/2006WR005389.

- Suchomel, B. J., B. M. Chen, and M. B. Allen III (1998), Network model of flow, transport and biofilm effects in porous media, *Transp. Porous Media*, 30(1), 1–23, doi:10.1023/A:1006560705680.
- Tang, Y., A. J. Valocchi, and C. J. Werth (2015), A hybrid pore-scale and continuum-scale model for solute diffusion, reaction, and biofilm development in porous media, *Water Resour. Res.*, 51, 1846–1859, doi:10.1002/2014WR016322.
- Taylor, A. R., S. Lamontagne, and R. S. Crosbie (2013), Measurements of riverbed hydraulic conductivity in a semi-arid lowland river system (Murray–Darling Basin, Australia), *Soil Res.*, 51(5), 363, doi:10.1071/SR13090.
- Thullner, M. (2010), Comparison of bioclogging effects in saturated porous media within one- and two-dimensional flow systems, *Ecol. Eng.*, 36(2), 176–196, doi:10.1016/j.ecoleng.2008.12.037.
- Thullner, M., and P. Baveye (2008), Computational pore network modeling of the influence of biofilm permeability on bioclogging in porous media, *Biotechnol. Bioeng.*, 99(6), 1337–1351, doi:10.1002/bit.21708.
- Thullner, M., J. Zeyer, and W. Kinzelbach (2002), Influence of microbial growth on hydraulic properties of pore networks, *Transp. Porous Media*, 49(1), 99–122, doi:10.1023/A:1016030112089.
- Thullner, M., M. H. Schroth, J. Zeyer, and W. Kinzelbach (2004), Modeling of a microbial growth experiment with bioclogging in a two-dimensional saturated porous media flow field, *J. Contam. Hydrol.*, 70(1–2), 37–62, doi:10.1016/j.jconhyd.2003.08.008.
- Thullner, M., P. Regnier, and P. Van Cappellen (2007), Modeling microbially induced carbon degradation in redox-stratified subsurface environments: Concepts and open questions, *Geomicrobiol. J.*, 24(3–4), 139–155, doi:10.1080/01490450701459275.
- Treese, S., T. Meixner, and J. F. Hogan (2009), Clogging of an effluent dominated semiarid river: A conceptual model of stream-aquifer interactions, *J. Am. Water Resour. Assoc.*, 45(4), 1047–1062, doi:10.1111/j.1752-1688.2009.00346.x.
- Ulrich, C., S. Hubbard, J. Florsheim, D. O. Rosenberry, S. Borglin, M. Trotta, and D. Seymour (2015), Riverbed clogging associated with a California Riverbank Filtration System: An assessment of mechanisms and monitoring approaches, *J. Hydrol.*, 529(3), 1740–1753, doi:10.1016/j.jhydrol.2015.08.012.
- van Genuchten, M. T. (1980), A closed-form equation for predicting the hydraulic conductivity of unsaturated soils, *Soil Sci. Soc. Am. J.*, 44(5), 892, doi:10.2136/sssaj1980.03615995004400050002x.
- White, D. C., and D. B. Ringelberg (1998), Signature lipid biomarker analysis, in *Techniques in Microbial Ecology*, edited by R. S. Burlage, pp. 255–289, Oxford Univ. Press, N. Y.
- Wingender, J., T. R. Neu, and H.-C. Flemming (1999), What are bacterial extracellular polymeric substances?, in *Microbial Extracellular Polymeric Substances*, edited by J. Wingender, T. R. Neu, and H.-C. Flemming, 258 pp., Springer, Berlin.
- Xie, Y., P. G. Cook, P. Brunner, D. J. Irvine, and C. T. Simmons (2013), When can inverted water tables occur beneath streams?, *Groundwater*, 52(5), 769–774, doi:10.1111/gwat.12109.
- Zhang, Y., S. Hubbard, and S. Finsterle (2011), Factors governing sustainable groundwater pumping near a river, *Ground Water*, 49(3), 432–444.